Impacts of nanofiller shapes on the interface confinement effect in polymer nanocomposites

Guotong Wang[1], Ruijie Wang[1*], Liya Wang[1], Chengyuan Wang[2], Ying Luo[1], Faling Zhang[1], Ziyu Wang[3], Chun Tang[1*]

1. Faculty of Civil Engineering and Mechanics, Jiangsu University, Zhenjiang 212013, P.R. China
2. Faculty of Science and Engineering, Swansea University, Bay Campus, Swansea, Wales SA1 8EN, UK
3. The Institute of Technological Sciences, Wuhan University, Wuhan 430072, P. R. China

Abstract Shape effect of nanofillers (NFs) on the properties of nanocomposites has attracted considerable attention in recent research. The present study aims to examine how NF shapes influence the confinement effect of polymer-NF interface on the physical properties of nearby polymer (the interphase). Herein molecular dynamics simulations are performed to capture the shift of interphase properties when NFs change from nanosphere to nanocylinder and nanofilm geometry. A stress analysis is then carried out in the interphase to identify a key parameter for characterizing the stress-property coupling and revealing the pathway of the NF shapes to impact the interphase properties. It is shown that the peak hydrostatic stress σ_{hyd} quantifies the effect of internal stresses on the properties of the interphase. Specifically, the shape transition considered can substantially enhance the peak σ_{hyd} by flattening the stress space in the interphase without largely affecting the polymer-NF interaction. Increased peak σ_{hyd} in turn upshifts the interphase properties and thus, leads to the coupling between the NF shapes and interface confinement effect.

Keywords: Nanofiller shape effect, curvature of nanofiller surface, polymer-nanofiller interface, interfacial confinement, hydrostatic stress

Email: tangchun@ujs.edu.cn; wangruijie@usj.edu.cn

1. Introduction

Polymer nanocomposites (PNCs) are synthesized by filling polymer matrix with nanofillers (NFs) of different shapes, e.g., gold nanoparticles [1], silver nanowires [2], carbon nano-tubes (CNTs) and -cones [3, 4], and nanosheets [5-7]. It has been reported [8-18] that NF shapes play an important role in determining and tuning PNC properties that have a broad range of applications in electrical/thermal conductivity, stress/strain sensing and actuation, energy harvesting/storage, self-healing capability, and electromagnetic interference shielding [19]. The NF shape effect on PNC properties thus becomes a major topic of great interest in recent research.

In existing studies [8, 12, 18], the shape effect on rheological properties was examined for various PNCs. For the PNCs filled with X- and Y-shaped graphene junctions, buckyball and nanodiamond, it was found [8] that different surface area-to-volume ratios of these NFs modify the NF-polymer interaction energy, which in turn changes the viscous properties of PNCs. The NF shape effect on the PNCs with fumed silica, colloid silica and the grafted colloids was also investigated and found to play a significant role in determining the percolation threshold of the NF-polymer network and thus, its viscoelastic properties [12]. Recently, for the PNCs filled with nanoparticles, nanorods and nanosheets, the nanorods were found to most efficiently raise the viscoelastic modulus among the three NFs due to its largest specific surface area and constraint of the interfacial interaction on polymer chain motility [18].

Efforts were also made to study the shape effect on the mechanical properties of PNCs [9, 10, 15, 16]. The MD simulations found that the rod-like NFs are the better toughening agent than spherical and triangular NFs due to the formation of stronger polymer crosslinks between NFs [9]. Recently, a multiscale MD-finite element model was developed, which showed that the fully curved NFs results in the decreased rate of

enhancement of PNC elastic properties [15]. In addition, an experimental study revealed that clay and CNTs are associated with the highest mechanical property improvement as compared with $CaCO_3$, talc and nano-crystalline cellulose [10]. The shape effect observed here was mainly attributed to the variation of the polymer-NF interfacial area [10]. Also, in the tensile tests of PNCs [16] the nanoplatelets used were shown to exert more significant toughening effect than nanospheres as the energy dissipation and toughening processes change substantially with the NF shapes. Along with the rheological and mechanical properties, NF shape effect was also examined for the conductivity [13] and other functionalities [14, 17] where the shape effect was shown to arise from the varying aspect ratios of the NF shapes considered [13, 14].

The above review has manifested the substantial effect of NF shapes on a range of material properties of various PNCs. Currently, the geometric parameters of NF shapes, e.g., the aspect ratio, surface area and area-to-volume ratio are recognized as key factors [8, 10, 11, 13, 18] that affect the polymer-NF interfacial van der Waals (vdW) interaction and thus change the properties of PNCs. Nevertheless, how these factors yield the shape effect on PNCs still remains unclear as 'NF shape−interfacial vdW interaction−PNC property' relation and the rationale behind it have not yet been explored in detail. On the other hand, the interphase generated by the interface confinement effect [20-23] was shown to significantly affect the material properties of bulk PNCs [24-26], which stimulated considerable efforts to measure interphase properties [27-34]. Moreover, it was discovered [28,35,36] very recently that the interfacial interaction yields a peak compressive stress in the interphase which controls the interphase properties and serves as the physical origin of the polymer-NF interface confinement effect [21, 32-34, 37]. These studies suggest that the NF shape transition may significantly change the stress concentration in the interphase and result in the

shape-dependent interphase properties, which would eventually impact the properties of PNCs via the percolation process. Thus, the study of NF shape effect on the interphase properties or the interface confinement effect offers an opportunity to bring an in-depth understanding of the NF shape effect on PNC properties. Previous study [11] only reported the NF shape effect on the mobility of the interphase polymer. Efforts need to be made to consider many other interphase properties and disclose the mechanism behind the coupling between NF shape and interphase properties.

Motivated by this idea, the present study examines the NF shape effect on interphase properties by first considering the mass density profile and glassy transitional temperature (T_g). In doing this, nanosphere, nanocylinder and nanofilm-like fillers are considered and the physical mechanisms behind the shape effect are investigated. Herein, the full-atom MD simulations are performed and complemented by the cohesive zone model [38-41] and continuum mechanics theories [42] to study the shape effect on the confinement effect and gain new insights into it via stress analyses.

2. Methodology

2.1 Molecule dynamics simulations

Three types of representative volume elements (RVEs) are considered for composite systems composed of polyethylene (PE) and gold (Au) NFs of different fundamental geometrical shapes, i.e., nanoparticle, nanopillar and nanoflake, which are respectively modelled as nanospheres, circular nanocylinders and rectangular nanofilms. To build the PE-NF composite RVEs we have first constructed a 500 monomer-long PE chain and the NFs of three different shapes. The obtained PE chains are then packed into a supercell with one NF inside. Herein, the volume of the supercell is $10\times10\times10nm^3$,

$10 \times 12 \times 12 nm^3$ and $12 \times 12 \times 14 nm^3$ for nanosphere, nanocylinder and nanofilm, respectively. The local energy minimum of the structure obtained by energy minimization using the conjugate gradient method then produces the initial PE-NF system RVE structural model. For each type of supercell, the nanofiller is placed within the polymer matrix volume where the nanoparticle is positioned at the cell center; the nanopillar is placed at the cell center with the axial direction aligned to a coordinate direction and finally the nanofilm is laid on the bottom of the cell within the z-plane (Fig. 1). The characteristic diameter of nanoparticle, nanopillar and the thickness of nanoflake are fixed at $5nm$. The initial packing mass density of PE is selected as $0.46 g/cm^3$ which can speed up the convergence of the equilibration process by avoiding high-energy initial configurations.

Here a full atom model is employed where the COMPASS force field [43] describes the interaction between the PE atoms and the embedded atom method (EAM) potential [44] captures the interactions among Au atoms. The 12-6 Lennard-Jones (L-J) potential is chosen for the non-bonded interaction between the Au and PE atoms. The nonbonded van der Waals (vdW) interactions is truncated at $1nm$ [45]. The values of the parameters used for all three interaction potentials are summarized in Table S1. MD simulations are performed via the large scale atomic/molecular massively parallel simulator (LAMMPS) [46] using the velocity Verlet algorithm with a timestep of $1fs$ and the periodic boundary conditions are used in all directions to eliminate the finite size effect.

The equilibrium state of the RVE is achieved at finite temperature in a two-stage process. First, the conjugate gradient method is used to find a local energy minimum of the RVE under the employed potentials. Then simulated annealing is performed where the system is initially thermalized at $500K$ for $1ns$ under the NVT ensemble and subsequently under the NPT ensemble at $1atm$ for another $1ns$. The equilibrated system

is subsequently cooled from 500K to 100K under the NPT ensemble within a 2ns period and further thermalized for another 2ns under the NPT ensemble at 100K. Fig. 1(a-c) shows the RVEs of the equilibrium NF-PE composite system during each step of the annealing procedure (for simplicity, the H atom is not shown in the figure). Such an annealing process is necessary to ensure that the equilibrated NF-PE system obtains structural properties in agreement with experimental (and existing simulation) values [28, 35, 47]. After the equilibrium process, the volume of the three initial RVEs finally reduce to $8.2\times8.2\times8.2nm^3$, $10\times10.3\times10.3nm^3$ and $12\times12\times11.5nm^3$, respectively. In this study, the dilute solution assumption [40, 41] is used, where the interaction between adjacent NFs is negligible. It is noted that uncertainty in computational results may arise due to different initial conditions at the same NF size, as such three simulations are performed for each Au-PE composite system and the resulting average properties are then used in the subsequent analysis and trend evaluation.

2.2 Continuum mechanics models

2.2.1 Cohesive zone model for the PE-NF interface

The components of polymer-NF composite system are illustrated in Fig. 1(d) to (f), i.e., the NF, polymer-NF interface (i.e., the vdW interaction induced gap) and the polymer matrix. The thickness of the interface (or the equilibrium vdW interaction distance) is denoted by h for the three systems shown in Fig. 1(d) to (f). As stated in previous studies [21, 28, 32-37], the polymer in the vicinity of the interface is constrained by the interfacial vdW interaction, which eventually leads to the formation of an interphase region between the interface and bulk polymer. In the interphase, the mass density, the glassy transitional temperature and the elastic modulus differ substantially from their bulk values due to the interface confinement effect.

To quantitatively study the vdW interaction between NFs and PE matrix, a cohesive zone model is used as shown in Fig. 1(d) to (f) where the yellow body represents the NF, the gray area is the surrounding polymer and the white area between the NF and polymer marks the NF-polymer interface. The vdW interaction energy between NF atom and PE united atom (the CH_2 group is treated as a united atom) is given by Lennard-Jones (L-J) potential function $\Omega(\mathcal{H}) = 4\beta\{(\alpha/\mathcal{H})^{12} - (\alpha/\mathcal{H})^{6}\}$. Here $\mathcal{H}$ denotes the distance between two atoms, α and β are the distance at $\Omega(\mathcal{H}) = 0$ and the energy well depth, respectively.

The cohesive energy between the two differential elements of NF-material with volume dV_{NF} and matrix with volume dV_m is $\Omega(\mathcal{H}) \cdot (\rho_{NF} dV_{NF}) \cdot (\rho_m dV_m)$ where ρ_{NF} and ρ_m are the densities of the NF and matrix, respectively. The cohesive energy between a differential element of the matrix and the NF can then be calculated by

$$d\Phi = \rho_m dV_m \iiint \Omega(\mathcal{H})(\rho_{NF} dV_{NF}) \tag{1}$$

For the nanosphere-polymer system, Eq. (1) can be expressed as follows [38-40].

$$d\Phi = \rho_m dV_m \int_0^{\pi} \int_0^{2\pi} \int_0^{r_{NP}} \Omega(\mathcal{H}) \cdot \rho_{NF} dV_{NF} = \rho_m dV_m \rho_{NF} \Phi_0(r) \tag{2}$$

Here, r is the radial distance of the reference point in polymer from the center of nanosphere, r_{NP} is the radius of the nanosphere (i.e., $r \geq r_{NP} + h$) and the specific form of $\Phi_0(r)$ can be found in Supporting Information S1.

Based on the Eq. (2), the cohesive energy $\Phi(h)$ of the whole system can be calculated as a function of h.

$$\Phi(h) = \int_{r_{NP}+h}^{\infty} 4\pi r^2 \rho_m \rho_{NF} \Phi_0(r) dr \tag{3}$$

In Eq. (3), the integral function gives the cohesive energy $\phi_{sur}(r)$ of a spherical polymer surface with radius r and surface density $\rho_m \times 1\mathring{A}$, i.e.,

$$\phi_{sur}(r) = 4\pi r^2 \rho_m \rho_{NF} \Phi_0(r) \tag{4}$$

The corresponding cohesive force on the polymer surface can then be calculated by

$$\frac{\partial \phi_{sur}}{\partial r} = 4\pi r^2 \left(\rho_m \rho_{NP} \frac{\partial \Phi_0}{\partial r}\right) + \frac{\partial (4\pi r^2)}{\partial r} \rho_m \rho_{NP} \Phi_0 \quad (5)$$

The equivalent radial force per unit area on a spherical polymer surface of radius r is finally obtained based on Eq. (5).

$$\sigma_{eq} = \frac{1}{4\pi r^2} \frac{\partial \phi_{sur}}{\partial r} = \rho_m \rho_{NF} \frac{\partial \Phi_0}{\partial r} + \rho_m \rho_{NF} \frac{\Phi_0}{r} \quad (6)$$

Similarly, based on Eq. (1), the equivalent radial force per unit area on a cylindrical polymer surface in nanocylinder-polymer system (Fig. 1(e)) is given by

$$\sigma_{eq} = \rho_m \rho_{NF} \frac{\partial \Phi_1}{\partial r} + \rho_m \rho_{NF} \frac{\Phi_1}{r} \quad (7)$$

and the equivalent force acting on a polymer plane in nanofilm-polymer system (Fig. 1(f)) can be calculated by

$$\sigma_{eq} = 4\pi\beta \rho_m \rho_{NF} \left(-\frac{\alpha^{12}}{5z^{10}} + \frac{\alpha^6}{2z^4}\right) \quad (8)$$

Herein z is a perpendicular distance of the reference point in polymer to the nanofilm surface. Eqs. (7) and (8) are derived in Supporting Information S2 and S3.

Next let us calculate the profile of σ_{eq}, i.e., the distribution of the vdW forces applied to the PE by the three NFs considered along the radial (r) direction of the nanosphere or nanocylinder (Fig. 1(d) and (e)), or the z-direction of the nanofilm (Fig. 1(f)). Here σ_{eq} is shown as a function of d (The distance from the NF surface measured along the direction perpendicular to the surface) in Fig. 2 where a high repulsive force per unit area (negative) around -200MPa is obtained for all three systems at $d \approx 0.26nm$. The repulsive force then decreases with rising d and becomes zero at $d \approx 0.28nm$. After that the cohesive force turns out to be an attractive force (positive) which rises to its peak value at $d = 0.325nm$. It then declines and approaches zero at sufficiently large d. It is noted that the maximum of the cohesive force per unit area is around 91.2MPa for all three NFs considered with the relative difference less than 10%.

2.2.2 Stress characterization of the matrix

To understand the action of the cohesive force on the matrix, the polymer matrix is considered as an infinite body. Here, the matrix is subjected to a body force σ_{eq} (i.e., the NF-polymer interaction shown in Fig. 2). In general, PE is a hyper-elastic material with complex constitutive relations. However, assuming that the stress and strain of the PE close to the interface are lower than the yield stress and strain (Fig. S1), we can approximately treat the PE as an elastic body with a linear constitutive relation. In addition, traction free boundary conditions are imposed on the inner polymer surface facing NFs and the outer polymer surface at infinity.

In the nanosphere-polymer system, the polymer confined by the interfacial interaction estimated by σ_{eq} (Eq. (6)) can be considered as a hollow and spherical elastic body (Fig. S2). The governing equation for the mechanical responses of the spherically symmetric structure is given as follows [42]

$$\frac{d}{dr}\left[\frac{1}{r^2}\frac{d}{dr}(r^2u)\right] = \frac{(1+\nu)(1-2\nu)}{E(1-\nu)} \cdot \sigma_{eq} \tag{9}$$

where u denotes the displacement function, E and ν represent the Young's modulus and Poisson's ratio of PE, respectively. In this analysis we have used the bulk material properties of PE measured in MD simulations (Supporting Information S4). The mass density variation shown in Fig.3(a) however has not been considered. Solving Eq. (9), we have obtained the displacement function of PE matrix.

$$u = u_0(r) + C_1 r + \frac{C_2}{r^2} \tag{10}$$

Here, C_1 and C_2 are the constants of integration. The specific form of $u_0(r)$ is shown in Supporting Information S5.

The perpendicular and parallel stresses on the spherical PE surface with radius r can be obtained based on Eq. (10), geometric equations and constitutive equations [42].

$$\sigma_{rr} = \frac{E}{(1+\nu)(1-2\nu)}\left[(1-\nu)\frac{du}{dr} + 2\nu\frac{u}{r}\right]$$

$$= \rho_m \rho_{NP} \Phi_0(r) + \frac{E(1-\nu)}{(1+\nu)(1-2\nu)} C_1 - \frac{E(1-\nu)}{(1+\nu)(1-2\nu)} \left[\frac{u_0}{r} + C_1 + \frac{C_2}{r^3}\right] \tag{11}$$

$$\sigma_{\theta\theta} = \sigma_{\varphi\varphi} = \frac{E}{(1+\nu)(1-2\nu)} \left[\nu \frac{du}{dr} + \frac{u}{r}\right]$$

$$= \nu\left(\frac{(1+\nu)(1-2\nu)}{E(1-\nu)} \rho_m \rho_{NP} \Phi_0(r) + C_1\right) - (1-2\nu)\left[\frac{u_0}{r} + C_1 + \frac{C_2}{r^3}\right] \tag{12}$$

For the problem considered, σ_{rr} satisfies the following boundary conditions.

$$\begin{cases} \sigma_{rr}|_{r=r_{NP}+h} = 0 \\ \sigma_{rr}|_{r\to\infty} = 0 \end{cases} \tag{13}$$

Substituting Eq. (11) into Eq. (13), we can calculate the values of C_1 and C_2 and finally obtain the analytical expressions of σ_{rr} and $\sigma_{\theta\theta}$.

By following a similar procedure, the stress fields of the polymer can also be obtained for the nanocylinder-polymer system (Eq. (14)) and nanofilm-polymer system (Eq. (15)), respectively. The derivations can be found in Supporting Information S6 and S7.

$$\begin{cases} \sigma_{rr} = \rho_m \rho_{NF} \Phi_1(r) - \rho_m \rho_{NF} \frac{1-2\upsilon}{1-\upsilon} \frac{1}{r^2} \int r \Phi_1(r) dr - \frac{C_3}{r^2} \\ \sigma_{\theta\theta} = \frac{\upsilon}{1-\upsilon} \rho_m \rho_{NF} \Phi_1(r) + \rho_m \rho_{NF} \frac{1-2\upsilon}{1-\upsilon} \frac{1}{r^2} \int r \Phi_1(r) dr + \frac{C_3}{r^2} \\ \sigma_{zz} = \frac{\upsilon}{1-\upsilon} \rho_m \rho_{NF} \Phi_1(r) \end{cases} \tag{14}$$

and

$$\begin{cases} \sigma_{zz} = 4\pi\beta \rho_m \rho_{NF} \left(\frac{\alpha^{12}}{45z^9} - \frac{\alpha^6}{6z^3}\right) \\ \sigma_{xx} = \sigma_{yy} = 4\pi\beta \rho_m \rho_{NF} \frac{\upsilon}{1-\upsilon} \left(\frac{\alpha^{12}}{45z^9} - \frac{\alpha^6}{6z^3}\right) \end{cases} \tag{15}$$

3. Results and discussions

The MD simulation procedure outlined in Sec. 2 shall be used to initially characterize the influence of NF shapes on the confinement effect of the PE-NF interface. Effort will then be made to identify the dominant mechanical parameter capable of quantifying the impact of the interfacial vdW interaction-induced stresses on the interphase properties

and shed light on the physical mechanisms leading to the NF shape effect based on the continuum mechanics theory described in Sec. 2.

3.1 Shape effect on the interphase properties

Herein, we shall characterize the material properties of the polymer confined by the nanoscale interface between polymer matrix and the embedded nanosphere, nanocylinder and nanofilm shown in Fig. 1(a), (b) and (c), respectively. The emphasis will be placed on the dependence of the interphase properties on NF shapes or the shapes of the polymer-NF interface. The models of the three PE-NF systems are illustrated in Fig. 1(d), (e) and (f), respectively, where Cartesian coordinates for all three systems and the corresponding spherical and cylindrical polar coordinates for the polymer-nanosphere and polymer-nanocylinder/nanofilm systems are shown in detail.

To exam the impacts of the NF shape on the interface confinement effect, we shall first measure the mass density profile of the interphase in the direction perpendicular to the surfaces of three types of NFs, i.e., the r (radial) directions of the nanosphere (Fig. 1(d)) and nanocylinder (Fig. 1(e)) and z-direction of the nanofilm (Fig. 1(f)). The method used can be found in Refs. [35, 36]. For all the three NFs, the results presented in Fig. 3(a) show the sinusoid density profiles in the interphase where three peak densities are observed. Here, the smooth curves for density profiles are obtained by adopting the spline functions to fit the MD simulation data shown in Fig. S3. It is noted that the three peak values, i.e., peak I, II and III (Fig. 3(a)) and their increase relative to the bulk value $0.9 g/cm^3$ (Fig. 3(b)) grow substantially during the shape transition considered. For example, the increase of density at peak I relative to the bulk value is found to rise from 62% to 71% and 89%, respectively when the nanosphere, nanocylinder and nanofilm are considered. In other words, the confinement effect measured by the relative increase of peak density I is improved by nearly 6% and 17%

when a nanosphere additive is replaced by the nanocylinder and nanofilm. A qualitatively similar NF shape effect can also be observed for peak density II and III in Fig. 3(b) where the relative increases can be raised by 6% and 16% (peak II), and 3% and 18% (peak III), respectively, due to the NF shape changes, which are comparable to those associated with peak density I.

With the density profile variation established, the corresponding T_g is then evaluated based on the MD simulations in Fig. 3(c) for the interphase I and II (Fig. 3(a)) formed in the PE matrix near the three types of NFs considered. Herein, interphase I represents an annulus region between the inner surface of polymer (a spherical PE surface where the PE mass density first reaches its bulk value) and a spherical PE surface which is 0.2 nm from the polymer inner surface. Interphase II is an annulus with a thickness of 0.7 nm and its inner surface coincides with the outer surface of interphase I. It is noted that similar to the trend of the peak density shown in Fig. 3(b), T_g calculated for the interphase I (blue filled rectangles) and II (red rectangles) increases substantially as NF geometry transitions from nanosphere to nanocylinder and nanofilm. To give a representative example here, T_g (= 311K) of interphase I associated with the nanosphere is found to be 31K higher than T_g (= 280K, Fig. S4) of bulk PE, which can be further enhanced by 16% (45K) and 24% (68K) via the NF shape change from the nanosphere to nanocylinder and nanofilm, respectively.

As shown above, the nanosheets produce the highest T_g for the interphase, which is followed by T_g associated with the nanocylinders and nanospheres, respectively. Since polymer monomer mobility is necessary for phase transition into an amorphous state [21] the higher T_g of polymer obtained should correspond to the slower mobility of the monomers. Thus, the increase of T_g due to the shape changes observed in the present full-atom MD simulations is in consistency with the observation in the previous coarse-

grained MD simulations [11] where the similar shape transition leads to the slower mobility of the polymer monomers. Indeed, the shape change-induced larger constraints on polymer chains [11] can explain the shape effect on the interface confinement effect achieved in the present study.

During the NF shape changes, the resulting higher peak mass density may also enhance the elastic modulus of the polymer. The statement is supported by previous studies where the interphase with higher density usually possesses an elastic modulus much higher than its bulk polymer values [28, 32]. This observation implies that NF shapes that modify the peak interphase density would also have a significant impact on the elastic modulus. Furthermore, the shape change-induced variation of the mass density in the interphase may likely be accompanied by the alterations in the effective energy barrier of electron tunneling of the interphase, as the mean distance between the monomer molecule is non-trivially reduced.

In summary, the NF shape can substantially impact the nanoscale confinement of the PE-NF interface and thus significantly alter the physical properties of the confined polymer. Since the interphase properties may largely affect the material behavior and properties of the bulk PNCs via the percolation process, the NF shape effect on the interphase properties obtained here may bring in a deeper understanding of the NF shape effect on the material properties of bulk PNCs [8-18]. Specifically, the NF shapes have the potential to become an effective parameter to control and tune a range of material properties of PNCs [8-12], e.g., mass density, T_g, elastic modulus, electrical conductivity, and piezo-resistivity of PNCs.

3.2 Role of the hydrostatic stress in shape effect

As mentioned above, the NF shape effect on the motility of the confined polymer or

the interphase was explained by the change of the total vdW force on the polymer due to the variation of NF shapes [11]. Recent studies [28, 35, 36] further indicated that the external vdW force generates a concentrated internal compressive stress within the polymer adjacent to NFs. It is this highly localized internal stress concentration that controls the properties of confined polymer and leads to the formation of the interphase with increased density and improved T_g relative to its bulk value. Thus, the coupling between NF shape and the interface confinement effect (as measured through the interphase properties changes) observed in Sec. 3.1 should be established by means of the localized internal stress concentration. Herein, the overall effect of internal stresses on material should be characterized by a parameter that reflects the synergistic effect of multiple components in the stress tensor, instead of the role of the individual components, and remains constant for all different coordinator systems selected. Thus, in what follows, an attempt shall be made to identify a frame independent, generalized parameter based on stress tensor to efficiently quantify and understand the overall impacts of interphase stresses on its material properties. To achieve this goal, we shall utilize the stress parameters defined based on the invariants of stress tensor, i.e., the hydrostatic stress related to the first stress tensor invariant [42]

$$\sigma_{Hyd} = (\sigma_1 + \sigma_2 + \sigma_3)/3 \tag{16}$$

and the Von Mises stress σ_{VM} related to the second stress tensor invariant [42],

$$\sigma_{VM} = \sqrt{\frac{1}{2}[(\sigma_1 - \sigma_2)^2 + (\sigma_1 - \sigma_3)^2 + (\sigma_2 - \sigma_3)^2]} \tag{17}$$

where σ_i (i = 1, 2 and 3) represents the principal stresses. Indeed, σ_{Hyd} and σ_{VM} can reflect the overall effects of stress states on the material at reference point and do not change with the transformation of coordinator systems.

To obtain σ_{Hyd} and σ_{VM} for the system considered we first calculate the principal

stresses of the interphase induced by the vdW force exerted by the NFs. Herein, the continuum mechanics models detailed in Sec. 2.2 are utilized, where the cohesive force (per unit surface area) in Fig. 2 is considered as a body force acting on the polymer in the vicinity of the PE-NF interfaces. On this basis, we have obtained the normal stress components perpendicular to the PE-NF interfaces, i.e., σ_{rr} in Fig. 4(a) and (b) and σ_{zz} in Fig. 4(c), and those parallel to the interfaces, i.e., $(\sigma_{\theta\theta}, \sigma_{\varphi\varphi})$ in Fig. 4(a), $(\sigma_{\theta\theta}, \sigma_{zz})$ in Fig. 4(b) and $(\sigma_{xx}, \sigma_{yy})$ in Fig. 4(c). While the magnitudes of these principal stresses changes along the radial directions or the direction perpendicular to the interfaces, they remain constant along parallel directions due to the geometrical symmetry of the PE-nanosphere system (Fig. 4(a)), the circular cylindrical surfaces of the PE-nanocylinder system (Fig. 4(b)) and the flat surfaces of the PE-nanofilm system (Fig. 4(c)).

With the principal stresses obtained, the corresponding σ_{Hyd} and σ_{VM} can be calculated based on Eqs. (16) and (17) for the three PE-NF systems considered. As shown in Fig. 4(d), compressive σ_{Hyd} reaches its maximum value near the same radial position where the peak density is found. The maximum value increases from 89MPa to 98MPa and 108MPa sequentially for nanosphere, nanocylinder and nanofilm. Thus, the peak σ_{Hyd} associated with the nanosphere is enhanced by 10% and 21% as the NF shape changes to the nanocylinder and nanofilm. The dependence on shape is found to be in good correspondence with the incremental trend observed for the peak densities in Fig. 3(b) and T_g in Fig. 3(c). The von Mises stress σ_{VM} calculated is shown in Fig. 4(e) where the maximum σ_{VM} is also found at the same location where peak σ_{Hyd} occurs. However, the trend of the maximum σ_{VM} change with the NF shape differs substantially than those observed for the peak densities and T_g (Fig. 3(b) and (c), respectively). The above results suggest the strong correlation between σ_{Hyd} and the NF shape effect achieved, which in turn reveals the possible pathway of NF shape to

impact the confinement effect, i.e., the variation of NF shape modifies the vdW interaction acting on the interphase, which then changes the peak value of compressive σ_{Hyd} and thus, shift the material properties of the interphase. σ_{VM}, however, is not directly related to the shape effect of NFs on the interphase properties.

The theory proposed above can be understood based on the physical impacts of σ_{Hyd} and σ_{VM}on the polymer structures and dynamics. Herein σ_{Hyd} is responsible for the volume change of material. Thus, raising its magnitude leads to the decrease of the free volume of polymer and results in higher peak mass density at the point where the stress concentration is located. In the meantime, rising compressive σ_{Hyd} also imposes substantially greater constraints on the polymer chains, which reduces the mobility of polymer monomers and thus, further raises T_g of the confined polymer [48]. In fact, the reduced mobility of the polymer monomers due to the enhanced polymer-NF interaction in the NF shape transitions has been confirmed by the coarse-grained MD simulations [11]. On the other hand, σ_{VM} is not related to the volume change or the constraints on the movement of polymer chains but primarily captures the shear stresses/deformation and reflects the resulting shape changes in the polymer matrix.

Based on our simulations and theoretical analyses we can draw the conclusion that σ_{Hyd} can be employed a key parameter to characterize the influence of the internal stresses of the interphase on its material properties and thus quantify the impacts of the NF shape dependent interfacial vdW interaction on the interface confinement effect (or the interphase properties). Moreover, as noted above, the peaks in the magnitude of both σ_{Hyd} and σ_{VM} are achieved at the same location in the polymer confined by the PE-NF interfaces showing that the largest volume contraction and shape distortion of the polymer occur at the same location in the interphase. This unique feature may have potential impacts on the mechanical behavior and properties of the interphase.

The above discussion about the coupling between σ_{Hyd} and material property of the polymer confined by the PE-NF interface is conducted in the framework of continuum mechanics theory. It is thus necessary to validate the results based on the MD simulations. To this end, an atomic stress is computed as the average of the normal atomic stresses in the three coordinate directions shown in Fig. 1 (a), (b) and (c). The method used can be found in Refs. [28] and the results are shown in Fig. 5. It is found that the peak compressive stress is also obtained in interphase I at the location where the concentrated σ_{Hyd} is found (Fig. 4 (d)). In particular, the peak atomic stress is raised by 19% and 47% relative to the nanoparticle values when the filler shape changes to nanocylinder and nanofilm, respectively, in coherence with those given by the continuum mechanics theory. A point to note is that three peak atomic stresses are obtained (Fig. 5) corresponding to the three peak densities shown in Fig. 3(a) while the continuum mechanics models (Secs. 2.2.2) only produce one peak σ_{Hyd} in interphase I (Fig. 4(d)). The discrepancy suggests that Fig. 4(d) captures the initial polymer response to the introduction of the interfacial interaction upon NF embedding (here the real density profile is not considered) while Fig. 5 depicts the final equilibrium state of the polymer composite after full polymer relaxation and associated stress redistribution occurs. This dynamic process, however, cannot be observed based on continuum mechanics models and deserves to be studied in the near future based on atomistic simulations.

3.3 Mechanisms of the nanofiller shape effect

The critical role of the hydrostatic stress in the shape effect has been identified based on the continuum mechanics theory and confirmed by the MD simulations. In this section, an effort will be made to further reveal the mechanism via which the variation

of the NF shape finally results in the shift of the peak σ_{Hyd} that is responsible for the density and T_g changes of the interphase. In Eq. (16), σ_{Hyd} is the average of the three principal stresses including one stress perpendicular to the NF surfaces and two stresses parallel with the surfaces (Fig. 4(a) to (c)). Thus, the key issue here is (i) which principal stress (or stresses) is primarily responsible for the shift of peak σ_{Hyd} during the NF shape changes and (ii) why the principal stress (or stresses) identified in (i) shows high sensitivity to the NF shape changes.

To examine these issues, in Fig. 6(a) we have shown the profiles of the principal stresses perpendicular to the NF surfaces, i.e., σ_{rr} in Fig. 4(a) and (b), and σ_{zz} in Fig. 4(c). As shown in Fig. 6(a), peak compressive stresses are achieved at the location where peak σ_{Hyd} is found (Fig. 4(d)). The magnitudes are around -182MPa with relative difference of less than 10%. These results indicate that the peak compression perpendicular to the NF surface is not sensitive to the variation of NF shapes. Subsequently, the two principal stresses parallel with the NF surfaces are calculated in Fig. 6(b), i.e., $\sigma_{\theta\theta}$ and $\sigma_{\varphi\varphi}$ adjacent to the spherical interface (Fig. 4(a)), $\sigma_{\theta\theta}$ and σ_{xx} in the proximity of the cylindrical interface (Fig. 4(b)) and σ_{xx} and σ_{yy} right below the flat interface (Fig. 4(c)).

It is observed in Fig. 6(b) that the peak parallel stresses also coincide with the respective peak σ_{Hyd} and peak perpendicular stress location. Here the peak value of -75MPa is obtained for both σ_{xx} and σ_{yy} in front of the flat interface, which is 74% higher than -43MPa achieved for $\sigma_{\theta\theta}$ and $\sigma_{\varphi\varphi}$ in the vicinity of the spherical interface. Interestingly, for the cylindrical interface the peak $\sigma_{\theta\theta}$ (-34.3MPa) is only half of peak σ_{zz} (-67.9MPa). The former is close to the maximum $\sigma_{\theta\theta}$ and $\sigma_{\varphi\varphi}$, while the latter is not far from the maximum σ_{xx} and σ_{yy} (Fig. 6(b)). This observation can be explained

by the fact that the curvature of the cylindrical surface along θ direction is equal to the curvature of the spherical surface, and its curvature in the x-direction is identical to that of the flat surface. Thus, the peak parallel principal stresses are found to depend sensitively on the principal curvatures of the NF surfaces that are closely related to the shapes of the NFs.

These results indicate that, during the variation of NF shapes the shift of peak σ_{Hyd} observed is primarily attributable to the shift of the peak parallel stresses due to the curvature variations caused by the shape changes. The contribution to the shift of peak σ_{Hyd} from the peak perpendicular stresses however is trivial as they are insensitive to the curvature change. Accordingly, the process in which NF shapes affect the peak σ_{Hyd} can be described as follows: The variation of NF shapes is achieved via the changes of the principal curvatures of the NF surfaces which generate distinctively different peak parallel stresses in the interphase but do not largely affect the perpendicular stress. It is this parallel principal stress change that finally leads to the shift of peak σ_{Hyd}.

Herein the principal curvature changes in the shape transition plays a critical role in changing peak σ_{Hyd} to generate the shape effect. However, the reason why curvature change shifts peak σ_{Hyd} could be fundamentally different from the understanding gained in studying the size effect of NFs. In previous studies [41, 49, 50], it was found that the polymer-nanosphere interaction can be intensified by increasing the radius or reducing the surface curvature of the nanosphere. As a result, such a curvature decreases (i.e., the radius increase) of the NF leads to the upshift of the peak σ_{Hyd} and accordingly, the growth of the peak density and T_g of the interphase as shown in Fig. 7(a) and (b) based on our MD simulations. Thus, the curvature effect induced by the size changes modifies the interphase properties by weakening or strengthening the interfacial vdW interaction. The geometrical symmetry of the vdW force field and the resulted stress

field of the interphase, however, remains unchanged.

In contrast, the curvature effect arising from the shape changes does not necessarily lead to the substantial change in the strength of the vdW interaction (Fig, 2) but can entirely change the geometric symmetry of the interfacial interaction field and therefore, reshape the spatial distribution of the internal stresses of the interphase. The transition of the stress field from spherical symmetry to cylindrical symmetry and plane symmetry can be observed in Fig. 4(a) to (c) as a typical example. In such a process, while the corresponding curvature decrease does not largely affect the interfacial vdW force (Fig. 2) and the principal stress perpendicular to the NF surface (Fig. 6(a)) it substantially raises the two stresses parallel with the NF surfaces (Fig. 6(b)).

From the above analyses it is noted that the curvatures of NF surfaces may affect the hydrostatic stress σ_{Hyd} and thus, the physical properties of the interphase by means of (i) modifying the strength of interfacial interaction (in the size effect) and (ii) changing the symmetry of the stress field and thus, the parallel principal stresses (in the shape effect). In other words, the shape changes of NFs do not necessarily change the interfacial vdW interaction but can still substantially raise the peak σ_{Hyd} and thus upshift the interphase properties by straightening the stress space in the interphase.

Herein, it is understood that, in a differential volume element of the polymer matrix the stresses parallel with the NF surfaces (Fig. 4(a) to (c)) originates from the resistance of the surrounding polymer to the Poisson extension of the element induced by its perpendicular contraction due to the interfacial interaction. In particular, we have noticed that the smaller NF surface curvature leads to the less curved internal stress space in the interphase (Fig. 4(a) to (c)) and the stronger resistance of the neighboring polymer to the Poisson extension of the differential element, i.e., the higher parallel stresses in the interphase (Fig. 6(b)). The above analyses thus indicate that enhanced

constraints of neighboring polymer on the Poisson extension due to the decreasing curvature is the origin of the sensitivity of the parallel principal stresses to the curvature change. The theory proposed here brings new insights to the dependence of the parallel principal stresses and σ_{Hyd} on NF surface curvature that may change substantially with NF shapes. In addition, as the larger curvature corresponds to lower parallel principal stresses and peak σ_{Hyd} the theory also provides a possible explanation for the experimental observation that fully curved carbon nanotubes in polymer matrix give rise to the decreased rate of enhancement of PNC elastic properties [15].

4. Conclusions

This study aims to examine the influence of NF shapes on the confinement effect of the polymer-NF interface, identify key parameter that quantifies the overall impact of the internal stresses on the material properties of the interphase and reveal the physical mechanism via which NF shapes are coupled with the interfacial confinement effect or the interphase properties.

It is shown that NF shapes substantially impact the confinement effect of the polymer-NF interface on the nearby polymer or the interphase. As a result, when the NF shape changes from the nanosphere into nanocylinder and nanofilm, the peak density of the interphase upshifts by 6% and 17%, respectively. At the same time, T_g of the interphase I is raised by 16% and 24%, respectively. Such a shape effect of NFs may also occur for other material properties of the interphase which are correlated to the mass density, e.g., elastic modulus and the energy barrier of electron tunnelling. Specifically, the obtained NF shape-dependence of the interphase properties provides new insight into the mechanisms via which the shapes of NFs can finally exert influence

on the material properties of bulk PNCs.

Hydrostatic stress σ_{hyd} is identified as a critical parameter for quantifying the ability of the internal stresses to decrease the free volume in the interphase and impose restriction on the mobility of its polymer monomers. Thus, the magnitude of σ_{hyd} achieved in the interphase plays a critical role in creating the confinement effect of the polymer-NF interface, showing the strong coupling between the internal stress and material properties of the confined polymer.

The shape effect obtained during the transition of NFs from nanosphere to nanocylinder and nanofilm originates from the decrease of the individual principal curvatures of the NF surfaces, which changes the geometrical symmetry of the interfacial vdW force field and flattens the internal stress space of the interphase. This results in the substantial enhancement of the parallel principal stresses due to the greater constraints imposed by the neighboring polymer. Thus, even if the interfacial vdW interaction remains nearly unchanged the shape transition, by straightening the stress space of the interphase, can still substantially improve the peak σ_{hyd} and thus upshift the peak density and T_g as well as other properties of the interphase.

Acknowledgements

This work was supported by the National Natural Science Foundation of China (Grant no. 12072134) and Jiangsu Funding Program for Excellent Postdoctoral Talent (Grant no. 2022ZB664)

References

1. Kim Y, Zhu J, Yeom B, Di Prima M, Su X, Kim JG, et al. Stretchable nanoparticle conductors with self-organized conductive pathways. Nature 2013;500(7460):59-63.
2. Kim H-J, Thukral A, Yu C. Highly sensitive and very stretchable strain sensor based on a rubbery semiconductor. ACS Appl Mater Interfaces 2018;10(5): 5000-5006.
3. Wang B, Zhang K, Zhou C, Ren M, Gu Y, Li T. Engineering the mechanical properties of CNT/PEEK nanocomposites. RSC Adv 2019;9(23):12836-12845.
4. Taheri SS, Fakhrabadi MMS. Interphase effects on elastic properties of polymer nanocomposites reinforced by carbon nanocones. Comp Mater Sci 2022;201:110910.
5. Liu H, Li Y, Dai K, Zheng G, Liu C, Shen C, et al. Electrically conductive thermoplastic elastomer nanocomposites at ultralow graphene loading levels for strain sensor applications. J Mater Chem C 2016;4(1):157-166.
6. Liu R, He J, Zhang J, Wang L. Moiré Tuning of the dynamic behavior of a twisted bilayer van der Waals material resonator. ASME J Appl Mech 2022;89(12):121001.
7. Liu R, Wang L. Nonlinear forced vibration of bilayer van der Waals materials drum resonator. J Appl Phys 2020;128(14):145105.
8. Li Y, Kröger M, Liu WK. Nanoparticle geometrical effect on structure, dynamics and anisotropic viscosity of polyethylene nanocomposites. Macromolecules 2012;45(4):2099-2112.
9. A, G, SR, NK, T. Influence of nanoparticle size, loading, and shape on the mechanical properties of polymer nanocomposites. J Chem Phys 2012;137(21):214901.

10. Hassanabadi HM, Rodrigue D. Effect of particle size and shape on the reinforcing efficiency of nanoparticles in polymer nanocomposites. Macromol Mater Eng 2014;299(10):1220-1231.
11. Gao Y, Liu J, Shen J, Wu Y , Zhang L. Influence of various nanoparticle shapes on the interfacial chain mobility: a molecular dynamics. Phys Chem Chem Phys 2014;16(39):21372-21382.
12. Zhao D, Ge S, Senses E, Akcora P, Jestin J, Kumar SK. Role of filler shape and connectivity on the viscoelastic behavior in polymer nanocomposites. Macromolecules 2015;48(15):5433-5438.
13. Khalil1 R, Homaeigohar S, Häußler D, Elbahri M. A shape tailored gold-conductive polymer nanocomposite as a transparent electrode with extraordinary insensitivity to volatile organic compounds (VOCs). Sci Rep 2016;6(1):33895.
14. Wolf C, Angellier-Coussy H, Gontard N, Doghieri F, Guillard V. How the shape of fillers affects the barrier properties of polymer/non-porous particles nanocomposites: A review. J Membrane Sci 2018;556:393-418.
15. Doagou-Rad S, Jensen JS, Islam A, Mishnaevsky Jr L. Multiscale molecular dynamics-FE modeling of polymeric nanocomposites of reinforced with carbon nanotubes and graphene. Compos Struct 2019;217:27-36.
16. S, X, Wang J, Kan Z, Chen H, Fu W, et al. Role of poly(ethylene glycol) grafted silica nanoparticle shape in toughened PLA-matrix nanocomposites. Compos Part B-Eng 2019;168:398-405.
17. Špírková M, Hodan J, Konefał R, Machová L, Němeček, P., Paruzel A. The influence of nanofiller shape and nature on the functional properties of waterborne poly(urethane-urea) nanocomposite films. Polymers 2020;12(9):2001.
18. Luo D, Wu H, Li H, Zhang W, Zhang L, Gao Y. Effect of shape and size of

nanofillers on the viscoelasticity of polymer nanocomposites. Polymer 2022;246:124750.

19. Gibson RF. A review of recent research on mechanics of multifunctional composite materials and structures. Compos Struct 2010;92(12):2793-2810.
20. Chen L, Zheng K, Tian XY, Hu K, Wang RX, Liu C, et al. Double Glass Transitions and Interfacial Immobilized Layer in in-Situ-Synthesized Poly(vinyl alcohol)/Silica Nanocomposites. Macromolecules 2010;43(2):1076-1082.
21. Napolitano S, Glynos E, Tito NB. Glass transition of polymers in bulk, confined geometries, and near interfaces. Rep Prog Phys 2017;80(3):036602.
22. Genix AC, Bocharova V, Carroll B, Lehmann M, Saito T, Krueger S, et al. Understanding the Static Interfacial Polymer Layer by Exploring the Dispersion States of Nanocomposites. ACS Appl Mater Interfaces 2019;11(19):17863-17872.
23. Taheri SS, Fakhrabadi MMS. Interphase effects on elastic properties of polymer nanocomposites reinforced by carbon nanocones. Comput Mater Sci 2022;201:110910.
24. Hassanzadeh-Aghdama MK, Mahmoodia MJ, Ansarib R. Creep performance of CNT polymer nanocomposites -An emphasis on viscoelastic interphase and CNT agglomeration. Compos Part B-Eng 2019;168:274–281.
25. Hassanzadeh-Aghdam MK. Evaluating the effective creep properties of graphene-reinforced polymer nanocomposites by a homogenization approach. Compos Sci Technol 2021;209:108791.
26. Yu S, Yang S, Cho M. Multi-scale modeling of cross-linked epoxy nanocomposites. Polymer 2009;50(3):945–952.
27. Das N, Begam N, Ibrahim M, Chandran S, Padmanabhan V, Sprung M, et al. Viscosity and Fragility of Confined Polymer Nanocomposites: A Tale of Two

Interfaces. Nanoscale 2019;11:8546-8553.

28. Reda H, Chazirakis A, Behbahani AF, Savva N, Harmandaris V. Mechanical properties of glassy polymer nanocomposites via atomistic and continuum models: The role of interphases. Comput Methods Appl Mech Engrg 2022;395:114905.
29. Zhang WG, Emamy H, Betancourt BAP, Vargas-Lara F, Starr FW, Douglas JF. The interfacial zone in thin polymer films and around nanoparticles in polymer nanocomposites. J Chem Phys 2019;151(12):124705.
30. Power AJ, Remediakis IN, Harmandaris V. Interface and Interphase in Polymer Nanocomposites with Bare and Core-Shell Gold Nanoparticles. Polymer 2021;13(4):541.
31. Wang ZK, Lv Q, Chen SH, Li CL, Sun SQ, Hu SQ. Effect of Interfacial Bonding on Interphase Properties in SiO2/Epoxy Nanocomposite: A Molecular Dynamics Simulation Study. ACS Appl Mater Interfaces 2016;8(11):7499-7508.
32. Fankhänel J, Arash B, Rolfes R. Elastic interphase properties of nanoparticle/epoxy nanocomposites: A molecular dynamics study. Compos Part B-Eng 2019;176:107211.
33. Yang S. Interface and interphase of nanocomposites tailored by covalent grafting of carbon nanotube: hierarchical multiscale modelling. Int J Mech Sci 2022;220:107160.
34. Huang J, Zhou JJ, Liu MJ. Interphase in Polymer Nanocomposites. ACS Au 2022; 2:280−291.
35. Wang G, Wang R, Wang C, Tang C, Luo Y, Xiao D. Mechanistic pathway of NP-polymer interface to engender nanoscale confinement. Compos Commun 2022;32:101186.
36. Wang G, Wang R, Wang C, Tang C, Zhang L. Active responses of nanoparticle-

polymer interface/interphase via the interfacial interaction redistribution. Int J Mech Sci 2023;243:108030.

37. Genix AC, Bocharova V, Carroll B, Lehmann M, Saito T, Krueger S, et al. Understanding the static interfacial polymer layer by exploring the dispersion states of nanocomposites. ACS Appl Mater Interfaces 2019;11(19):17863-17872.
38. Jiang L, Huang Y, Jiang H, Ravichandran G, Gao H, Hwang KC, et al. A cohesive law for carbon nanotube/polymer interfaces based on the van der Waals force. J Mech Phys Solids 2006;54(11):2436-52.
39. Zhao J, Jiang J, Jia Y, Guo W, Rabczuk T. A theoretical analysis of cohesive energy between carbon nanotubes, graphene and substrates. Carbon 2013;57:108-19.
40. Zhao J, Lu L, ZhangZ, Guo W, Rabczuk T. Continuum modelling of the cohesive energy for the interfaces between films, spheres, coats and substrates. Comp Mater Sci 2015;96:432-438.
41. Wang Y, Wang C, Wang G, Wang R. Effect of the surface curvature and volume fraction of AuPs on the AuP-matrix interface. Comp Mater Sci 2017;134:58–66.
42. Bower AF. Applied mechanics of solids. CRC Press, 2009.
43. Sun H. COMPASS: An ab initio force-field optimized for condensed-phase applications - Overview with details on alkane and benzene compounds. J Phys Chem B 1998;102(38):7338-7364.
44. Foiles M, Baskes MI, Daw MS. Erratum: Embedded-atom-method functions for the FCC metals Cu, Ag, Au, Ni, Pd, Pt, and their alloys. Phys Rev B 1988;37(17):10378.
45. Hossain D, Tschopp MA, Ward DK, Bouvard JL, Wang P, Horstemeyer MF. Molecular dynamics simulations of deformation mechanisms of amorphous polyethylene. Polymer 2010;51(25):6071–6083.

46. Plimpton S. Fast Parallel Algorithms for Short-Range Molecular Dynamics. J Comput Phys 1995;117(1):1-19.
47. Wang Y, Wang R, Wang C, Yu X. AuNP-PE interface/phase and its effects on the tensile behaviour of AuNP-PE composites. J Appl Phys 2018;123(21):214305.
48. Lu H, Tang Y, Cao X, Zhu P, Zou W, Li T, et al. The change of glass transition temperature under general stress state in amorphous materials. Extreme Mech Lett 2023;58:101951.
49. Emamy H, Kumar SK, Starr FW. Structural properties of bound layer in polymer–nanoparticle composites. Macromolecules 2020;53(18):7845–7850.
50. Cui W, You W, Yu W. Mechanism of mechanical reinforcement for weakly attractive nanocomposites in glassy and rubbery states. Macromolecules 2021;54(2):824–834.

Figures

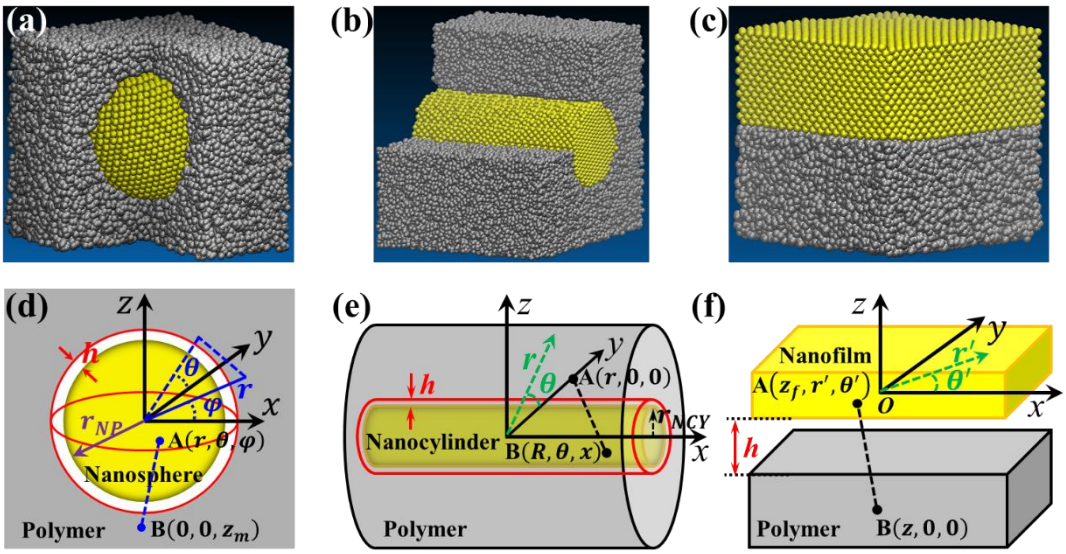

Fig.1 Molecular models of (a) PE-nanoparticle system, (b) PE-nanopillar system and (c) PE-nanosheet systems, and the corresponding mechanical models, i.e., (d) polymer-nanosphere interface model, (e) polymer-nanocylinder interface model and (f) polymer-nanofilm interface model. The Cartesian and polar coordinate systems are also shown there. Noted that, the *xy* plane of the Cartesian coordinate systems in (f) coincides with the bottom surface of the nanofilm.

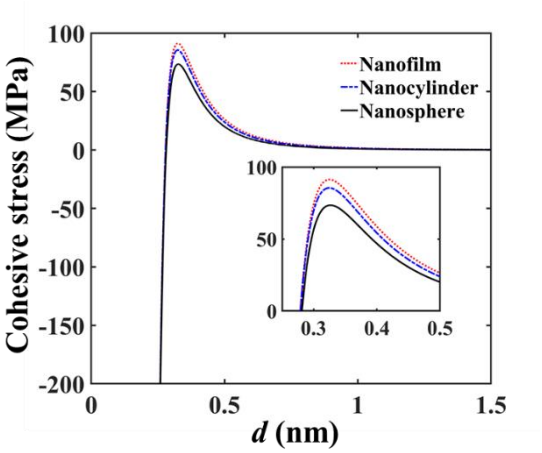

Fig. 2 Cohesive forces (per unit area) calculated as the functions of the perpendicular distance *d* to the surface of the nanosphere (black solid line), nanocylinder (blue dash-dotted line) and nanofilm (red dotted line), respectively.

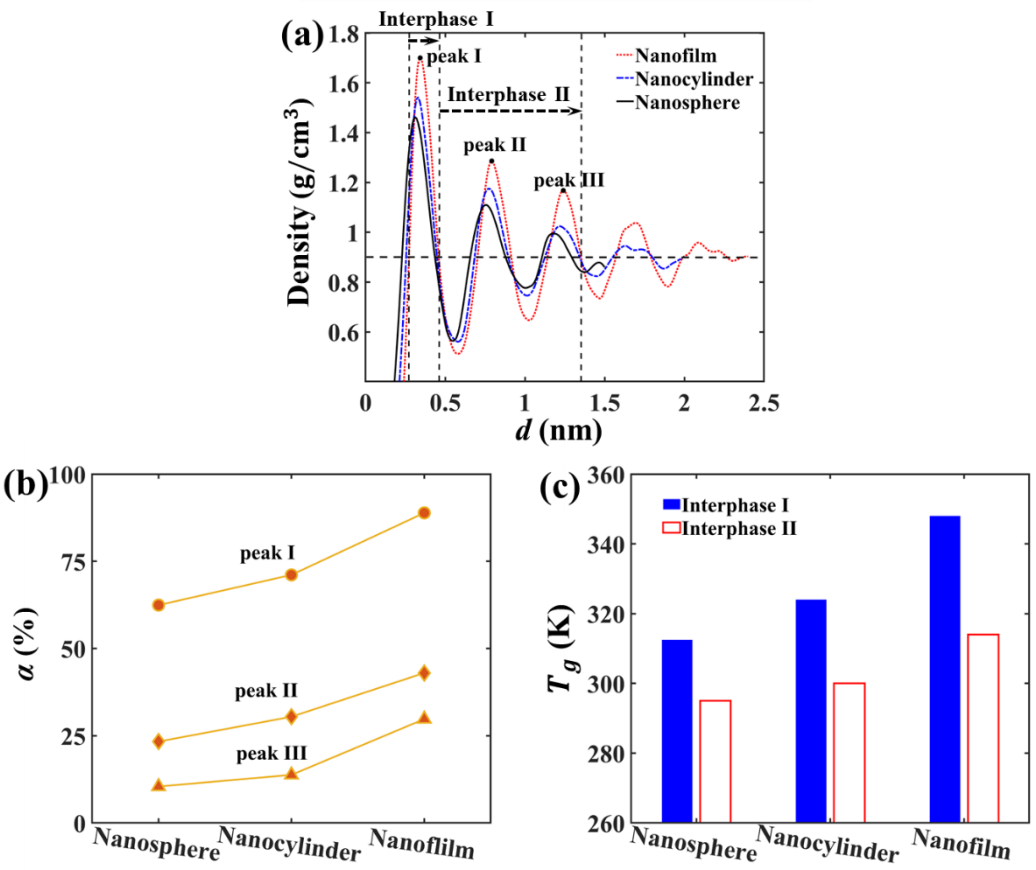

Fig. 3 (a) The mass density profile of the interphase and polymer matrix, (b) the relative increase α of the three peak mass densities relative to the bulk value and (c) the glass transition temperature T_g obtained for the interphase I and II associated with the nanosphere, nanocylinder and nanofilm, respectively.

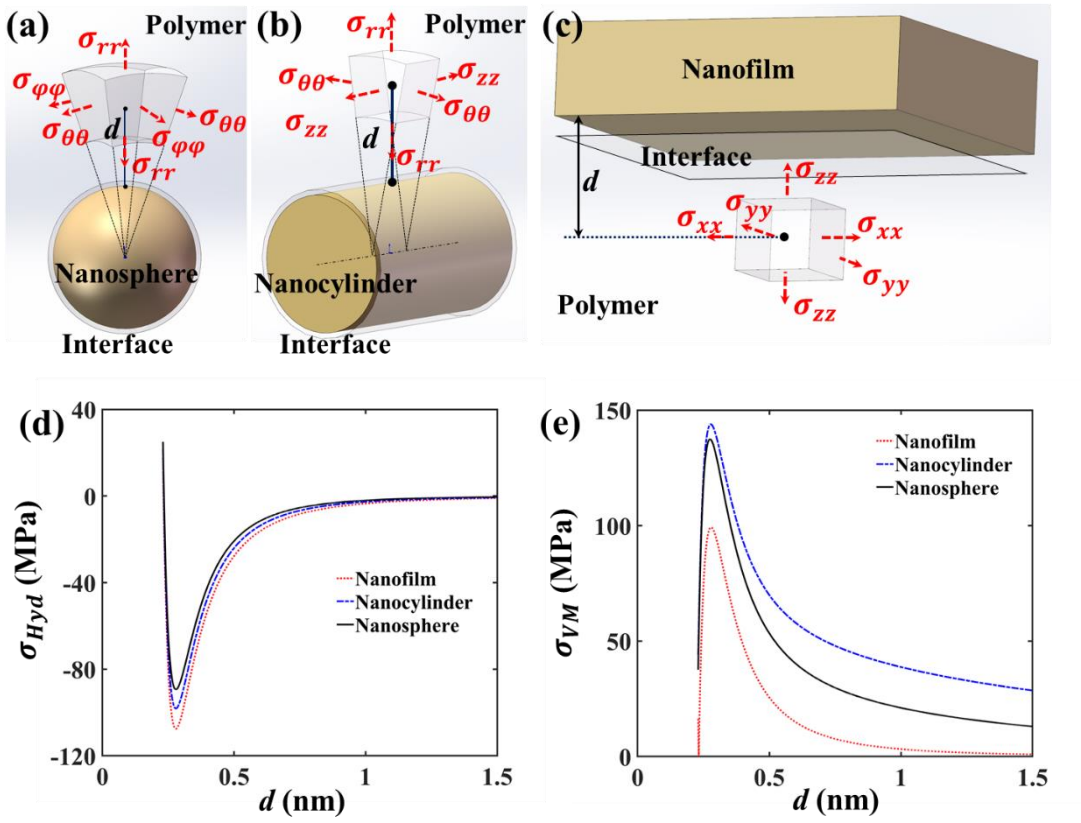

Fig.4 The principal stresses obtained in the interphase surrounding the (a) nanosphere, (b) nanocylinder and (c) nanofilm, respectively, and the profiles of (d) σ_{Hyd} and (e) σ_{VM} in the interphase in the vicinity of the above three types of NFs.

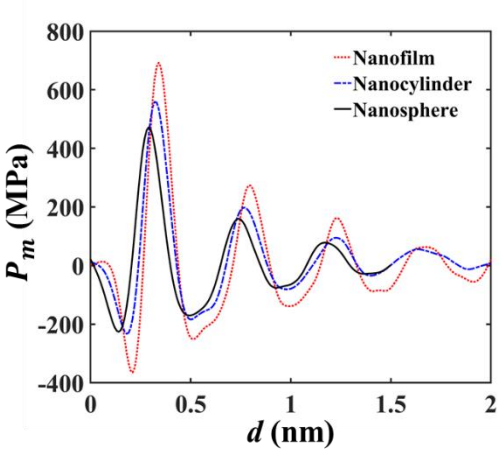

Fig.5 Atomic stresses P_m calculated as the functions of the perpendicular distance d to the surfaces of the three types of nanofillers, i.e., nanosphere, nanocylinder and nanofilm.

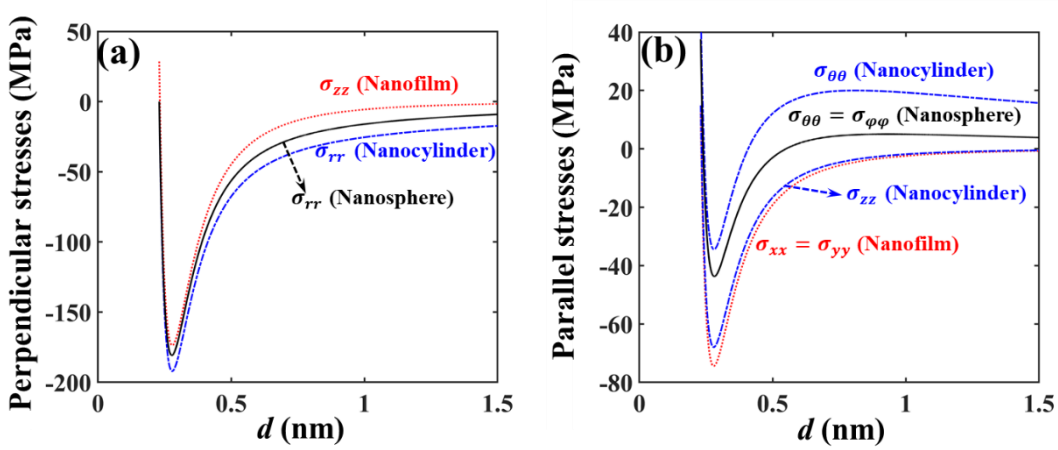

Fig.6 The principal stresses of the interphase (a) perpendicular to and (b) parallel with the interface between PE and nanosphere, nanocylinder and nanofilm, respectively.

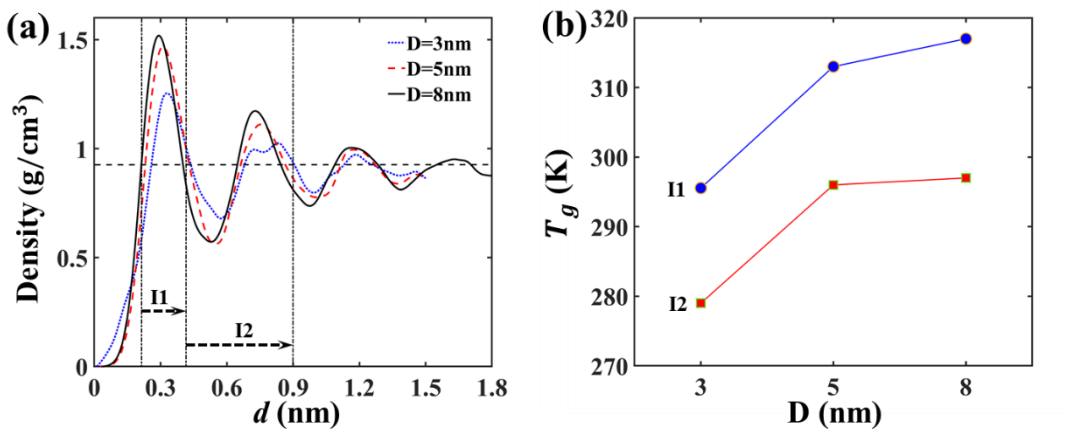

Fig.7 (a) Mass density profile and (b) glass transition temperature T_g obtained for two local interphases (I and II) shown in (a) in front of the interface between PE and nanosphere with diameter rising from 3*nm* to 5*nm* and 8*nm*.